Journal of Alloys and Compounds 823 (2020) 153617

Contents lists available at ScienceDirect

Journal of Alloys and Compounds

journal homepage: http://www.elsevier.com/locate/jalcom

Synthesis and characterization of Ag^{+} and Zn^{2+} co-doped $CaWO_4$ nanoparticles by a fast and facile sonochemical method

N.F. Andrade Neto [a, *], B.P. Dias [a], R.L. Tranquilin [b], E. Longo [b], M. Li [c], M.R.D. Bomio [a], F.V. Motta [a]

[a] LSQM – Laboratory of Chemical Synthesis of Materials, Department of Materials Engineering, Federal University of Rio Grande do Norte – UFRN, P.O. Box 1524, Natal, RN, Brazil
[b] CDMF-UFSCar, Universidade Federal de São Carlos, P.O. Box 676, São Carlos, SP, 13565-905, Brazil
[c] IFSC, USP, Av. Trabalhador São Carlens 400, CEP 13566-590 e, São Carlos, SP, Brazil

ARTICLE INFO

Article history:
Received 4 October 2019
Received in revised form
16 December 2019
Accepted 30 December 2019
Available online 31 December 2019

Keywords:
Sonochemical method
Ag and Zn co-doped $CaWO_4$
Photoluminescence
Photocatalysis

ABSTRACT

In this work, Ag^{+} and Zn^{2+} co-doped $CaWO_4$ nanoparticles were obtained by fast and facile sonochemical method. The nanoparticles were characterized by X-ray diffraction (XRD), Fourier transformed infrared spectroscopy (FTIR), Raman spectroscopy, scanning electron microscopy (SEM), transmission electron microscopy (TEM), visible ultraviolet spectroscopy (UV–Vis) and photoluminescence property. The photocatalytic activity was studied against methylene blue (MB) dye under sunlight and $CaWO_4$ powders were tested in 3 reuse cycles. The diffractograms indicate the non-formation of secondary phases and the Rietveld refinement estimated the crystallite sizes, being 27.38, 19.89, 18.70 and 16.39 nm for the pure, Ag, Zn and Ag:Zn samples, respectively. SEM and TEM images showed that the particles are agglomerated and have a mean diameter ranging from 16.76 (Ag:Zn) to 71.76 nm (pure). Defects generated by doping shift the gap band to higher energies and act to prevent electron/hole (e^{-}/h^{+}) pair recombination, reducing photoluminescence and favoring $CaWO_4$ photocatalysis. Scavenger methodology indicated that h^{+} is the main mechanism acting in photocatalysis, and the reuse tests indicated that the silver-doped sample, even with the better initial response, loses efficiency over the course of the cycle, while the co-doped sample maintains efficiency, and is therefore indicated for reuse photocatalysis applications in methylene blue dye degradation.

1. Introduction

Environmental policies regarding industrial waste treatment become stricter with industrial advancement. Waste from the textile and food industries receives special attention due to the generation of organic and water-soluble waste, which harms the local fauna and flora [1]. Thus, treating these residues using advanced oxidative processes (AOP) based on heterogeneous photocatalysis is widely reported in the literature, where a semiconductor material acts as a catalyst in the photocatalytic process [2–5]. TiO_2 is the most studied semiconductor material because it has good photocatalytic properties and is non-toxic [6,7]. However, this material has limited properties, mainly due to its crystalline structure. Thus, materials that have a more complex structure, such as two different cations, are gaining attention.

Semiconductor materials of XWO_4 (X = Ca, Cu, Zn, Cd) structures are widely reported in the literature due to the excellent properties derived from their microstructure [8–11]. In heterogeneous photocatalysis, e^{-}/h^{+} pairs are generated when the semiconductor is excited by sufficient energy radiation to overcome its gap energy (Egap) [11]. If these charges do not recombine to their initial state, they migrate to the surface of the materials and react with the medium to generate reactive oxygen species (ROS), which have a high capacity for degradation of organic pollutants [12]. Among these materials, $CaWO_4$ has gained attention for photocatalytic applications due to its chemical and thermal stability, in addition to having a high direct Egap (~4.5 eV), making it difficult to recombine the e^{-}/h^{+} pairs [13–15].

Heterojunctions or doping are normally performed in order to improve $CaWO_4$ properties, thus altering the recombination rate of the photogenerated e^{-}/h^{+} pairs [15–17]. Zhang et al. [18] showed

* Corresponding author.
E-mail addresses: netoandrade@ufrn.edu.br, nfandraden@gmail.com (N.F.A. Neto).

https://doi.org/10.1016/j.jallcom.2019.153617
0925-8388/

that one way to optimize $CaWO_4$ photocatalytic activity is by synthesizing a biochar composite, which reduces the recombination of the electron/hole pairs photogenerated. Meanwhile, Huang et al. [19] showed that $CaWO_4$ co-doping with Er/Yb and Tm/Yb increases their photocatalytic activity by generating more O_2^- radicals. The mechanisms of $CaWO_4$ photocatalysis are little discussed in the literature, as most of the studies report the photoluminescent and electrochemical properties. In addition, the vast majority of works report rare-earth doping of $CaWO_4$. Thus, in this work transition metal ions (Ag^+ and Zn^{2+}) co-doped $CaWO_4$ nanoparticles were synthesized by the fast and facile sonochemical method, explaining the main photocatalytic mechanisms acting on pure and doped material and reusability against methylene blue cationic dye.

2. Materials and methods

Calcium nitrate ($Ca(NO_3)_2.4H_2O$ - Alfa Aesar, 98%), silver nitrate ($AgNO_3$ - Synth, 99%), sodium tungstate ($Na_2WO_42H_2O$ - Synth, 99.5%), zinc nitrate ($Zn(NO_3)_2.6H_2O$ - Sigma-Aldrich, 98%), polyvinylpyrrolidone (PVP - $(C_6H_9NO)_n$ - Vetec P.M. 40.000), ammonium hydroxide (NH_4OH – Synth, 30%) and deionized water were used as precursor materials.

A solution containing 2 mmol calcium nitrate, 10 mmol PVP and 40 mL deionized water (solution I) and a solution containing 2 mmol sodium tungstate, 10 mmol PVP and 40 mL deionized water (solution II) was initially prepared. Both solutions were kept under stirring for 10 min for complete homogenization. After this time, solution (I) was immersed in the solution (II) and stirred for 10 min, forming a transparent solution (solution III). Ammonium hydroxide was added for pH control, setting it to 10, making the solution a whitish color. The solution (III) was then taken to a Branson 102C ultrasonic tip (20 kHz) where it remained for 30 min. After ultrasonic treatment, the precipitate was centrifuged and washed with deionized water until pH neutralization. The powders were then dried for 24 h at 60 °C. Silver and zinc doped samples followed the same methodology, with silver nitrate and zinc nitrate stoichiometrically added at 4 mol% proportions to calcium nitrate in solution (I). The co-doped sample was performed using 2% silver and 2% zinc. The bare powder was named Pure, while the doped samples were named Ag, Zn and Ag:Zn, according to doping.

The powders were characterized by X-ray diffraction (Shimadzu, XRD-6000) using CuKα radiation (1.5418 Å), in which the powders were scanned from 10 to 90° using a speed of 1°/min and step of 0.02°. Rietveld refinement using the General Structure Analysis System (GSAS) program with graphical interface EXPGUI [20] was performed to obtain more crystallographic information. To do so, we used background, scale factor, microstructure, crystal, texture and strain parameters for refinement. The Fourier Transform Infrared (FTIR) technique was performed using the Shimadzu IRTracer-100 equipment, with scanning from 500 to 4000 cm^{-1}. The Raman scattering spectra were recorded at room temperature in the frequency range from 100 to 1200 cm^{-1} with a resolution of 2 cm^{-1} and 64 scans, using a VERTEX 70 RAMII Bruker spectrophotometer (USA) with a Nd:YAG laser (1024 nm) and the maximum output power kept at 100 mW. A scanning electron microscope (SEM) was used to observe the organization and morphology of the powders. Transmission electron microscopy (TEM) and high-resolution transmission electron microscopy (HRTEM) was performed in the FEI TECNAI G2 F20 microscope operating at 200 kV. The UV–Vis spectroscopy was performed on a Shimadzu UV-2550 equipment, with a wavelength range of 200–900 nm and programmed for the diffuse reflectance mode. Kubelka-Munk function [21] was applied to convert reflectance data in absorbance, and the Wood and Tauc methodology [22] was used to estimate the bandgap (Egap) energy. The photoluminescence (PL) measurements were obtained using a 325 nm laser at room temperature in a Mosospec 27 monochromator (Thermal Jarrel Ash, USA) coupled to an argon laser photomultiplier (Coherent Innova 90 K, USA).

2.1. Photocatalytic activity

The efficiency of the powders as catalyst was estimated by discoloration of the methylene blue (MB) dye at pH 5 and maximum absorbance at 664 nm. To do so, 5 mg of powder was maintained in contact with 50 mL of MB solution (10^{-5} mol L^{-1} concentration) under UV radiation. The powder was maintained in contact with the MB dye for 20 min to eliminate adsorbent effects. After this, the solutions were illuminated by six UVC lamps (TUV Philips, 15 W) for 120 min. The photocatalytic activity was then determined by the variation of the dye absorption bands in a Shimadzu UV-2600 spectrophotometer.

The mechanism acting on the photocatalytic process was determined by the use of charge, electron (e^-) and hole (h^+), and hydroxyl radical (·OH) scavengers. For this, isopropyl alcohol (1 mL alcohol/100 mL dye), EDTA (7.2 mg EDTA/100 mL dye) and $AgNO_3$ (8.5 mg $AgNO_3$/100 mL dye) were used to suppress the action of hydroxyl radicals (·OH), positive charges (h^+) and negative charges (e^-), respectively.

3. Results and discussion

Fig. 1a presents the diffractograms for the $CaWO_4$ samples obtained by the sonochemical method. According to the diffractograms, it can be seen that they align with the ICSD 15586 card, referring to the tetragonal crystalline system $CaWO_4$ and space group I 41/a. It is also observed that there was no formation of secondary phases. Fig. 1b shows an enlargement of the highlighted area in the diffractograms (Fig. 1a), referring to the main plane (112) of $CaWO_4$. It can be seen that it shifts to greater angles with the occurrence of doping, which is more evident for the silver-doped sample. Displacement of diffraction peaks to larger angles is usually associated with reduced interplanar crystal spacing [12]. Further crystalline information on doping in the $CaWO_4$ lattice was obtained through the Rietveld refinement. Fig. 2 presents the refined diffractograms for $CaWO_4$ samples, highlighting the difference between observed and theoretical values. Table 1 presents the crystallographic data obtained through the Rietveld refinement, as well as the refinement adjustment data.

The *Rp, chi², and R(F)²* are a quality parameter for evaluation of the Rietveld refinement quality. values close to 1 for the *Rp* and chi^2 and values below to 0.1 for $R(F)^2$ indicate a good refinement. In addition, visual analysis between observed and calculated curves allows this analysis. Thus, the data obtained from the Rietveld refinement have coherence. Ca^{2+} has an ionic radius of 0.106 nm, while Ag^+ and Zn^{2+} have an ionic radius of 0.113 and 0.083 nm, respectively. Even with greater ionic radius, the difference between the Ag^+ and Ca^{2+} valences promotes compression distortions in the $CaWO_4$ lattice, causing crystal size reduction to occur [23]. The changes resulting from doping can be seen in Table 1, where (according to the refinement) the *c/a* ratio of tetragonal crystals increases with silver doping, being in agreement with the reduction in interplanar spacing and consequent displacement of crystalline peaks. By looking at Fig. 2e and f, it is easy to visualize the W coordinates to four oxygen atoms, forming the tetragonal cluster $[WO_4]$, while Ca is coordinates to eight oxygen atoms, forming the cluster $[CaO_8]$. Such changes in the crystalline structure associated with the non-formation of secondary phase peaks indicate the correct incorporation of Ag^+ and Zn^{2+} ions into the $CaWO_4$ lattice.

Fig. 3a shows the Fourier transform infrared spectroscopy (FTIR)

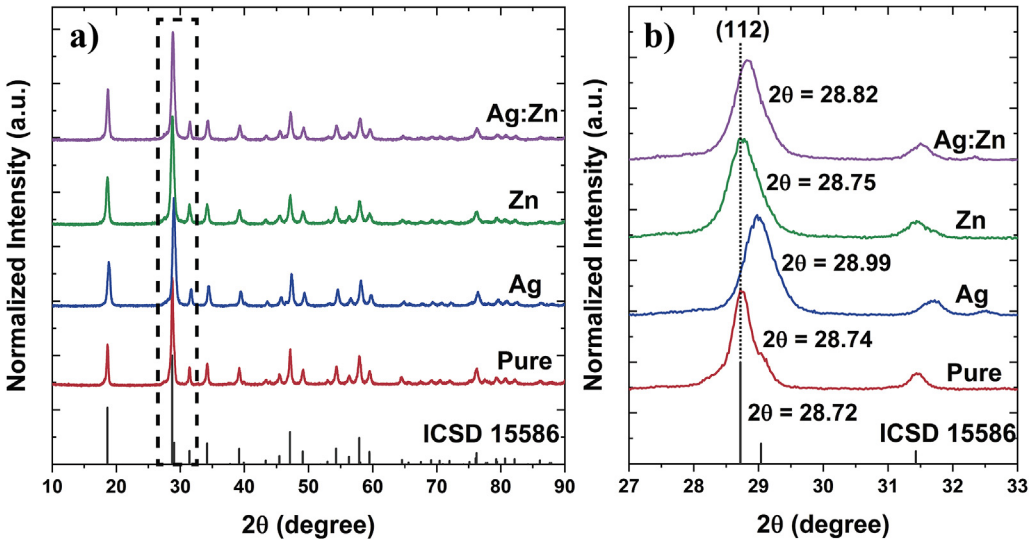

Fig. 1. (a) Diffractograms of $CaWO_4$ samples and (b) Diffractogram enlargement near plane (112).

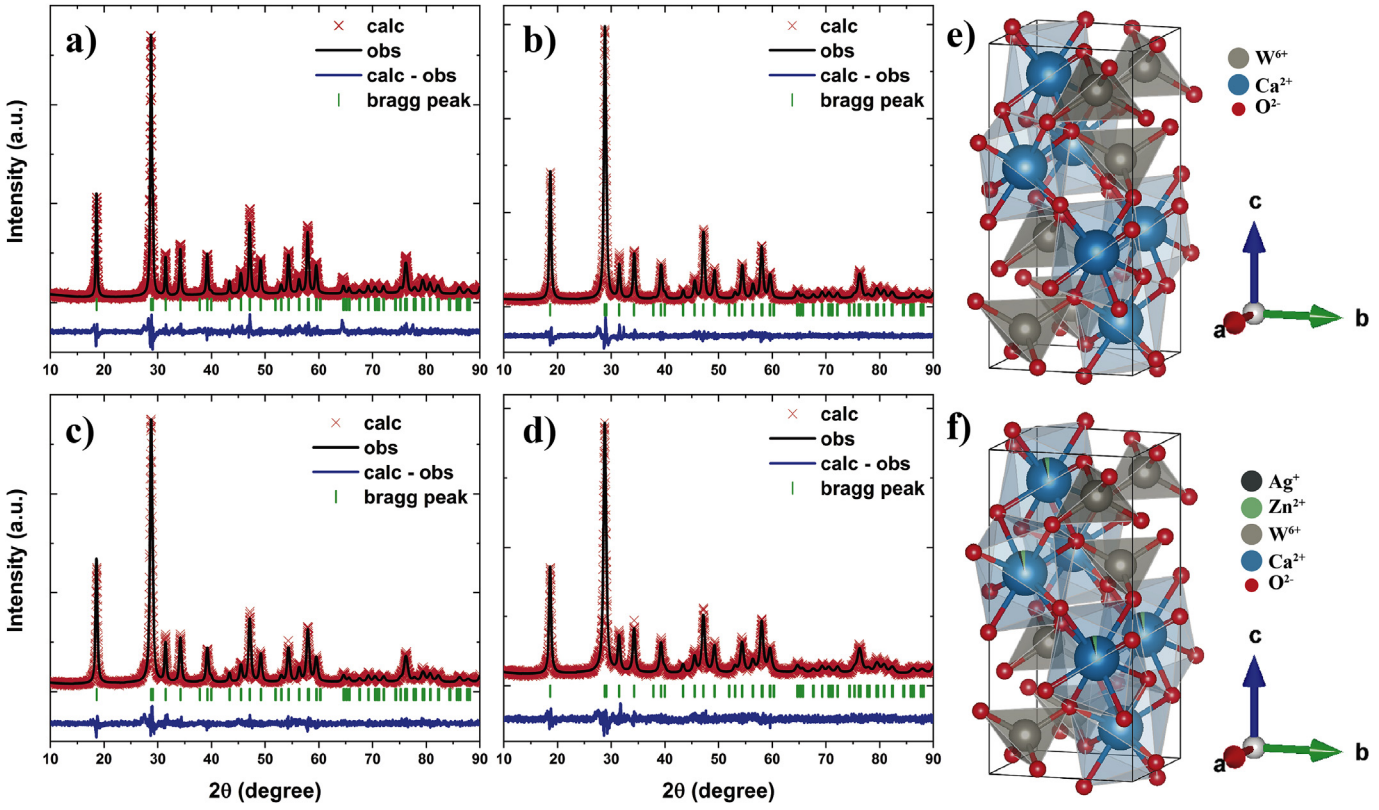

Fig. 2. Observed and calculated diffractograms obtained by the Rietveld refinement for (a) Pure, (b) Ag, (c) Zn and (d) Ag:Zn samples and tetragonal structure illustration for (e) Pure and (f) Ag:Zn samples.

spectra for the $CaWO_4$ powders. The wideband centered around 3400 cm^{-1}, as well as the band around 2300 cm^{-1}, present in all samples corresponds to the elongation vibrations between O—H for water molecules adsorbed on the surface of the powders [24]. The bands centered at 2930, 1649 and 1434 cm^{-1} correspond to the bonds between C—H_2, C—OH and C—O, indicating the presence of PVP surfactant on the surface of the powders [24]. The intense 760 cm^{-1} centering band is associated with asymmetric elongation vibration ($v3$) between O—W—O present in tetrahedron WO_4^{2-} [25]. As highlighted in Fig. 3a, silver doping generates the appearance of a band at 555 cm^{-1}, while zinc doping promotes the appearance of a band at 622 cm^{-1}, so these bands are associated with elongation vibrations between Ag—O and Zn—O, respectively.

Raman scattering spectroscopy was performed with frequency ranging from 100 to 1200 cm^{-1}. According to Silva et al. [26], broad vibrations mode in Raman spectra indicates a short-range structural disorder. Thus, the well-defined vibrations modes indicate a low level of defects in the $CaWO_4$ lattice. The bands at 910, 836, 794,

Table 1
Microstructural and refinement parameters obtained through GSAS software with EXPGUI interface.

Sample	Pure	Ag	Zn	Ag:Zn
a (A)	5.2439	5.2368	5.2413	5.2404
c (A)	11.3777	11.3797	11.3799	11.3794
Volume (A^3)	312.8695	312.0777	312.6198	312.4987
c/a	2.1697	2.1730	2.1712	2.1715
Rp	0.0892	0.0734	0.0716	0.0743
Chi^2	1.884	1.442	1.398	1.346
$R(F^2)$	0.0553	0.0425	0.0380	0.0439
Crystallite size (nm)	27.38	19.89	18.70	16.39
Microstrain	0.0003145	0.0004364	0.0004625	0.000526
% Ag	0	4.13	0	2.12
% Zn	0	0	4.71	2.21

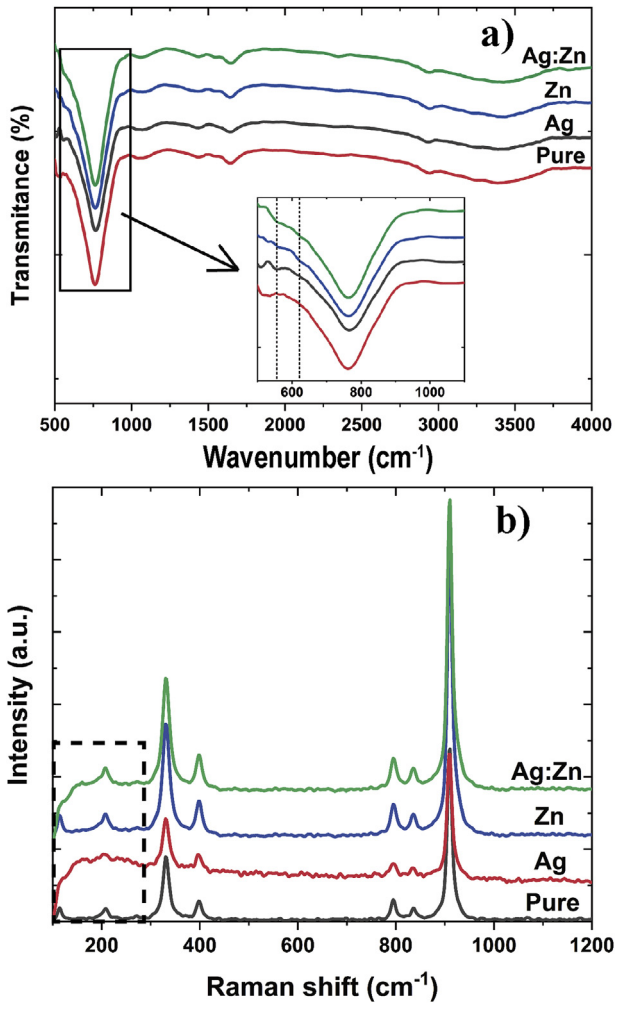

Fig. 3. (a) FTIR and (b) Raman spectra for $CaWO_4$ samples.

398, 330, 208 and 114 cm^{-1} are associated with the $CaWO_4$ tetragonal phase. The 910 cm^{-1} band is associated with the symmetrical elongation (*v*1) between W—O and the 330 cm^{-1} band is associated with the symmetrical elongation (*v*2) of the O—W—O. The band at 836 cm^{-1} corresponds to the anti-symmetric elongation (*v*3) and the band at 398 cm^{-1} corresponds to the anti-symmetrical elongation (*v*4) of the W—O [27]. The $CaWO_4$ scheelite group presents a strong covalent bond W—O forming the WO_4^{2-} ionic group and weak interaction with the Ca^{2+} cations [28]. The noise increase in Raman spectra for silver-doped samples is due to the defects generated in the $CaWO_4$ lattice, indicating the short-range structural disorder is more present in these samples.

More information about the $CaWO_4$ lattice defects was obtained through the symmetrical elongation peaks *v*1, between W—O, and *v*2, between O—W—O. For this, the peak was adjusted with the Gauss function in Origin software and are shown in Fig. S1 at supplementary material and the data are shown in Table 2. According to obtained data, the vibration mode *v*1 shifted to a lower frequency when doping with silver, while zinc doping and the codoped sample shifted to a higher frequency than the pure sample. While vibration mode *v*2 shifted to lower frequencies in all samples. The width at half height (FWHM) of vibration modes *v*1 and *v*2 increased for all doped samples over pure. Thus, the results are consistent with those shown in the XRD results, where an increase in disorder is expected with the replacement of Ca atoms by Ag and Zn.

Fig. 4 shows SEM images for $CaWO_4$ samples. As shown in Fig. 4a (Pure), there is the presence of micrometer-scale beads, and it is evident from the enlarged image that these beads are formed by misshaped morphology nanoparticles. Fig. 4b—d indicate that doping provides for a loss of tendency to form micrometer spheres where nanoparticles randomly agglomerate. The $CaWO_4$ nanoparticle size estimation was performed using ImageJ software [29]. The histograms obtained are shown in Fig. S2 in the supplementary material. As shown in the histograms, the pure sample has a mean diameter of 71.76 (±8.85) nm, while samples doped with Ag, Zn and Ag:Zn have diameters of 40.13 (±6.47), 42.05 (±9.69) and 16.76 (±2.53), respectively.

Small scale nanoparticle formation is easily accomplished by the sonochemical method. In this methodology, the generation and implosion of microbubbles generate high local temperature and pressure. This results in almost instantaneous nucleation of various crystallites, which are prevented from growing due to the rapid duration of temperature and pressure [1]. In addition, the use of PVP as a surfactant prevents crystal growth, favoring the formation of small-scale particles. According to Ávila-López et al. [30], the use of low concentration solutions favors forming irregularly shaped nanoparticles. Thus, the surfactant/precursor ratio (5:1) used in this work was sufficient to guarantee forming particles with small diameters. As highlighted in the Raman and DRX pattern, silver causes a large number of internal defects in the $CaWO_4$ lattice. These defects act to alter the surface energy of the crystals and consequently their growth, thus generating particles with smaller diameters (Fig. S1) and which clump together in order to reduce the surface energy.

Transmission electron microscopy (TEM) and high resolution (HRTEM) were performed due to the high agglomeration of the nanoparticles, as seen through the SEM images. Fig. 5 shows the images obtained for the pure (Fig. 5a) and Ag:Zn (Fig. 5b) samples, followed by the magnifications obtained by HRTEM. Via the images, the reduction in nanoparticle size is clearly observed by the co-doped sample, and the particles have no spherical character. The interplanar spacing was estimated using HRTEM images, obtaining values of 3.10 and 3.08 Å for the pure and Ag:Zn samples, respectively. Such spacings are characteristic of the (112) plane, which corresponds to the main plane of $CaWO_4$, as highlighted in Fig. 1.

Further information regarding the structural disorder obtained by Ag and Zn doping in the $CaWO_4$ lattice was obtained by ultraviolet—visible spectroscopy. Fig. 6a shows the absorption curves obtained by applying the Kubelka-Munk equation to the reflectance data. According to the obtained spectra, an increase in the absorption intensity as silver and zinc doping occurs is noticed, as well as the band shifting to shorter wavelengths, indicating higher absorption in the ultraviolet region. Absorption in the

Table 2
Position (x_c) and FWHM for the *v*1 and *v*2 symmetrical elongation peaks obtained through the GAUSS adjust.

Sample		Pure	Ag	Zn	Ag:Zn
*v*1	x_c (cm^{-1})	909.955	909.699	910.235	910.190
	FWHM	13.003	14.247	13.469	13.557
*v*2	x_c (cm^{-1})	331.015	330.495	330.887	330.866
	FWHM	16.168	17.661	17.662	17.672

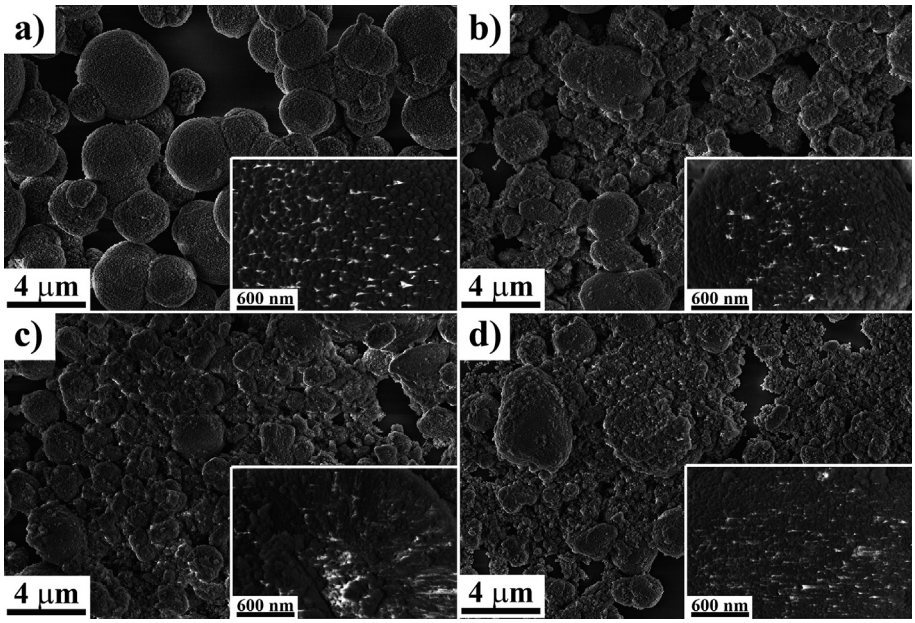

Fig. 4. SEM images for (a) Pure, (b) Ag, (c) Zn and (d) Ag:Zn samples.

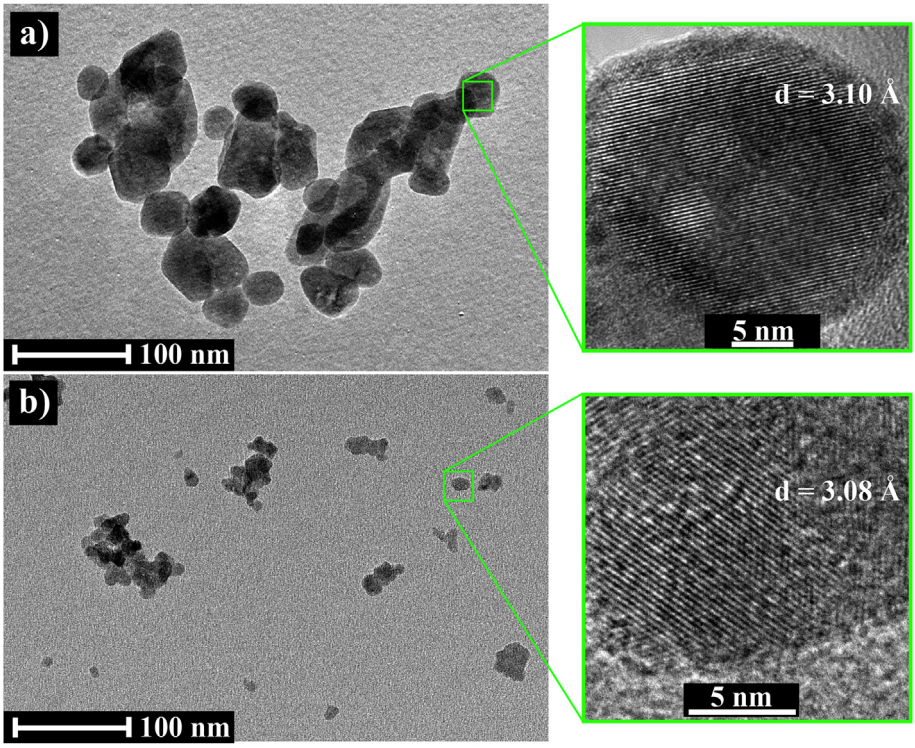

Fig. 5. TEM and HRTEM images for (a) Pure and (b) Ag:Zn samples.

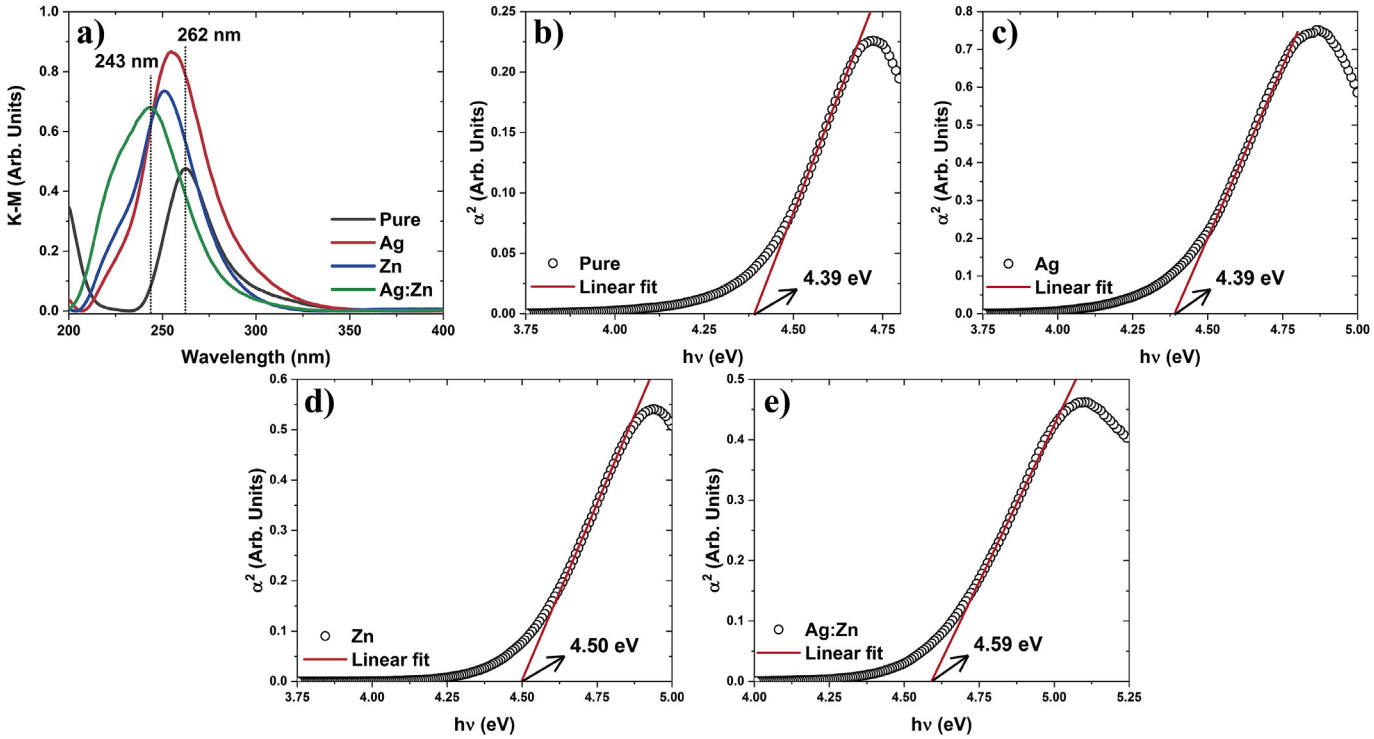

Fig. 6. Absorption spectrum obtained through the Kubelka-Munk equation and extrapolation of the linear portion of the α^2 curves by photon energy for (a) Pure, (b) Ag, (c) Zn and (d) Ag:Zn samples.

ultraviolet region is characteristic of $CaWO_4$ and is associated with charge transfer transitions from the 2p electron of oxygen entering the empty 5d tungsten orbitals in the WO_4^{2-} complex [31,32]. Thus, increased absorption accompanied by shifting to shorter wavelengths is associated with a higher level of defects in the $CaWO_4$ lattice as doping is performed.

Fig. 6b–e illustrate the curves obtained by extrapolating the linear portion of the curves obtained by the allowed direct transition [33], applying the Wood and Tauc model for estimating the bandgap (Egap) of the powders. Through these curves, the pure samples of Ag, Zn and Ag:Zn show Egaps of 4.39, 4.39, 4.50 and 4.59 eV, respectively. As shown in Fig. 6a, doping provides greater absorption in the ultraviolet region, indicating an increase in the energy required for exciting the valence band electron to the conduction band. The increase in Egap is probably associated with the Burstein-Moss effect, where defects generated by the insertion of silver and zinc occupy locations near the conduction band, shifting it to higher energy values [34].

Fig. 7a shows the photoluminescence spectra accompanied by their respective emission colors and Fig. 7b illustrates the position in the CIE diagram obtained for the $CaWO_4$ samples in this study. The pure sample shows the highest intensity and broadband centered at 500 nm, covering much of the visible spectrum. The $CaWO_4$ broadband is characteristic of $^3T_1$, $^3T_2 \rightarrow {}^1A_1$ transitions relative to WO_4^{2-} and WO_6^{6-} groups [35]. The photoluminescent capacity of the materials is directly related to the recombination velocity of the e^-/h^+ pairs, where the facilitation of this recombination generates higher photoluminescent intensities [36]. As shown above, doping promotes the appearance of $CaWO_4$ lattice defects; thus, these defects act as impediment centers for the recombination of e^-/h^+ pairs, reducing the material photoluminescence [37]. Silver-doped and silver-zinc-codoped samples have the lowest luminescent intensities due to the presence of silver, and their use is widely reported due to the creation of high impedance traps in the e^-/h^+ pair recombination [38]. In contrast to the reduction in luminescent intensity with silver doping, an increase in photocatalytic capacity is expected. The displacement of the absorption band with zinc doping occurs due to the emergence of oxygen vacancies, favoring emission in the blue region [38]. The coherence between the theoretical and emission colors can be observed with the assistance of the CIE diagram, as highlighted in Fig. 7a.

The photocatalytic activity of $CaWO_4$ powders was estimated by the variation of methylene blue dye concentration when subjected to UV radiation. Fig. 8a shows the curves of the variation in methylene blue dye concentration over the test time. The powders were initially maintained under agitation without the presence of light to eliminate the adsorptive effects. As seen in Fig. 8a, the silver-doped sample exhibits greater photocatalytic activity, completely reducing MB dye concentration after 120 min, while pure, Zn and Ag:Zn samples reduced the concentration by 25.99, 55.51 and 63.78%, respectively. Increased photocatalytic activity with silver and zinc doping are frequently reported in the literature [23,39–41]. Silver doping generates oxygen vacancies to balance the loads in the $CaWO_4$ lattice due to differences in valence with calcium. Even with calcium and zinc ions having the same valence, they have a different ionic radius, where zinc is smaller. This difference between the rays promotes the formation of internal strains, which hinder the movement of photogenerated e^-/h^+ pairs, improving photocatalytic activity. This can be proven by the reduction in photoluminescent activity as previously shown. As shown in the photoluminescent tests, oxygen vacancies act as impediment centers for e^-/h^+ pair recombination, reducing photoluminescence and favoring the migration of charges to the nanoparticle surface and generating more advanced oxidative species (ROS) to the dye surface oxidation. The photocatalytic kinetic constant was estimated by linearizing the catalytic data for better analysis of photocatalytic activity, as shown in Fig. 8b. The

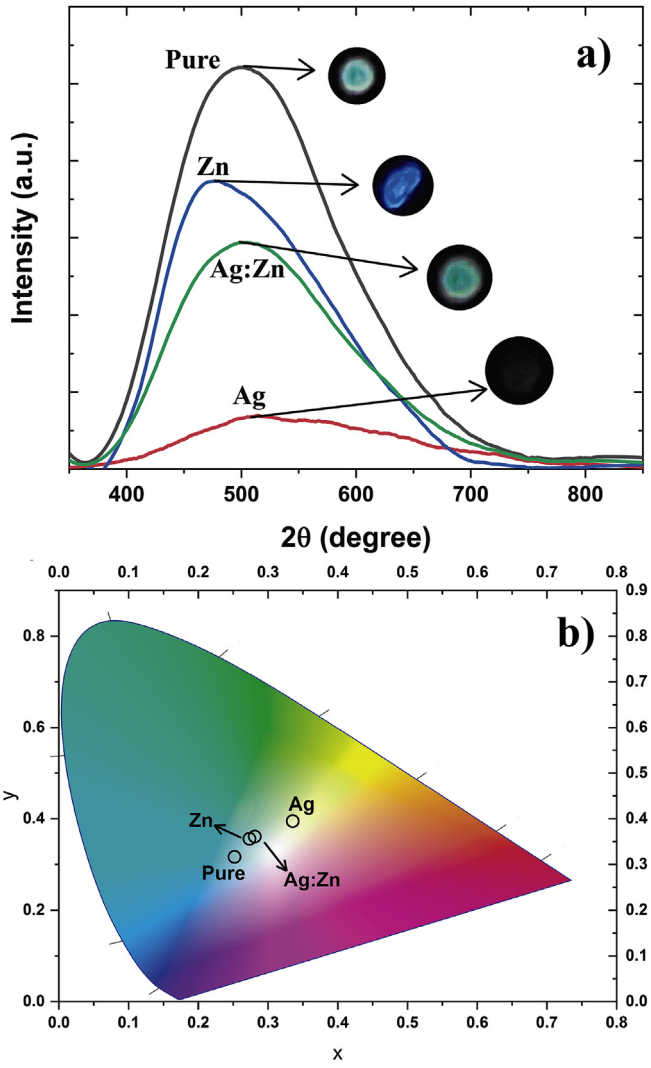

Fig. 7. (a) PL spectra and digital emission photography and (b) CIE diagram for $CaWO_4$ samples.

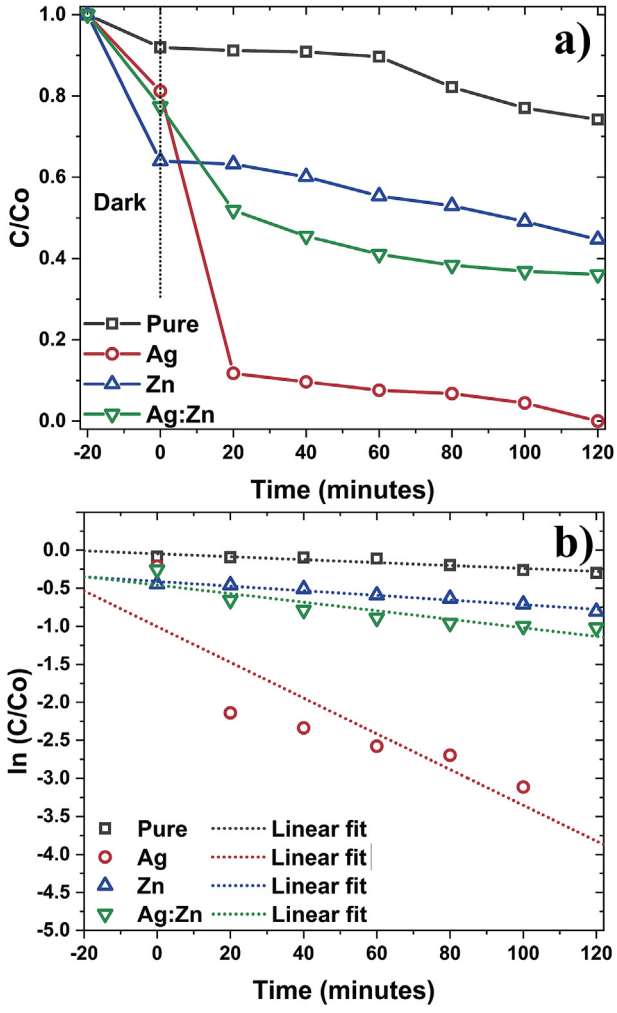

Fig. 8. (a) Variation of the methylene blue dye concentration (C/C_0) by the assay time and (b) your linearization ($\ln C/C_0$) for the determination of the photocatalytic kinetic constant. (For interpretation of the references to color in this figure legend, the reader is referred to the Web version of this article.)

kinetic constant determination occurred similarly to previous works [12,42]. Thus, kinetic constants $k = 0.28 \times 10^{-2}$, 5.46×10^{-2}, 1.21×10^{-2} and 1.79×10^{-2} min^{-1} were obtained for pure, Ag, Zn and Ag:Zn samples, respectively.

As seen in Fig. 8b, the linear fit does not fit the data well as photocatalytic efficiency is increased, indicating that doping acts to reduce the continuous linearity of the catalytic process. The reduction in linearity is associated with variation in dye molecule concentration, where greater interaction with nanoparticles initially occurs due to higher concentration, thus increasing the catalytic efficiency [43]. The kinetic constant acts as an important tool for estimating the catalytic behavior of semiconductor materials. The values obtained in this study illustrate the positive effect of doping, where catalytic kinetics increase by 20x when doping $CaWO_4$ with silver. The photocatalytic results are consistent with the photoluminescent analyzes, indicating that doping reduces the recombination rate of e^-/h^+ pairs, favoring photocatalytic activity.

As discussed earlier, doping causes defects in the $CaWO_4$ lattice which act to prevent the recombination of photoexcited e^-/h^+ pairs. The performance of these charges in photocatalysis was studied through the use of scavengers to better explain the photocatalytic mechanism. Thus, Fig. 9 shows the variation curves of MB dye concentration by the assay time using charge scavengers. To do so, $AgNO_3$ (AG), EDTA and isopropyl alcohol (ISO) were used to inhibit the action of e^-, h^+ and ·OH, respectively. Fig. 9a shows the curves for the pure sample, indicating that the use of scavengers increases dye degradation. This fact is consistent with photocatalytic and photoluminescent analyzes, where the pure sample presents a high recombination rate of the e^-/h^+ pairs so that by inhibiting one of these in isolation it will make the other available to act on generating reactive oxygen species (ROS), thereby increasing the photocatalytic activity of the powders. The effect of the isolated mechanisms is less evident for doped samples (Fig. 9b–d) which have a lower e^-/h^+ pair recombination rate due to the presence of defects in the material lattice.

The silver-doped sample (Fig. 9b) shows a reduction in photocatalytic activity with the addition of EDTA, indicating that holes play a major role in ROS generation. Similarly, zinc-doped and co-doped samples (Fig. 9c and d) indicate that holes play a major role in the photocatalytic process, but electrons also play a significant role. Thus, the results indicate that h^+ is the main mechanism acting in photocatalysis for all samples, being responsible for both directly oxidizing dye molecules on the surface of the powders, as well as interacting with the environment and generating hydroxyl radicals [44].

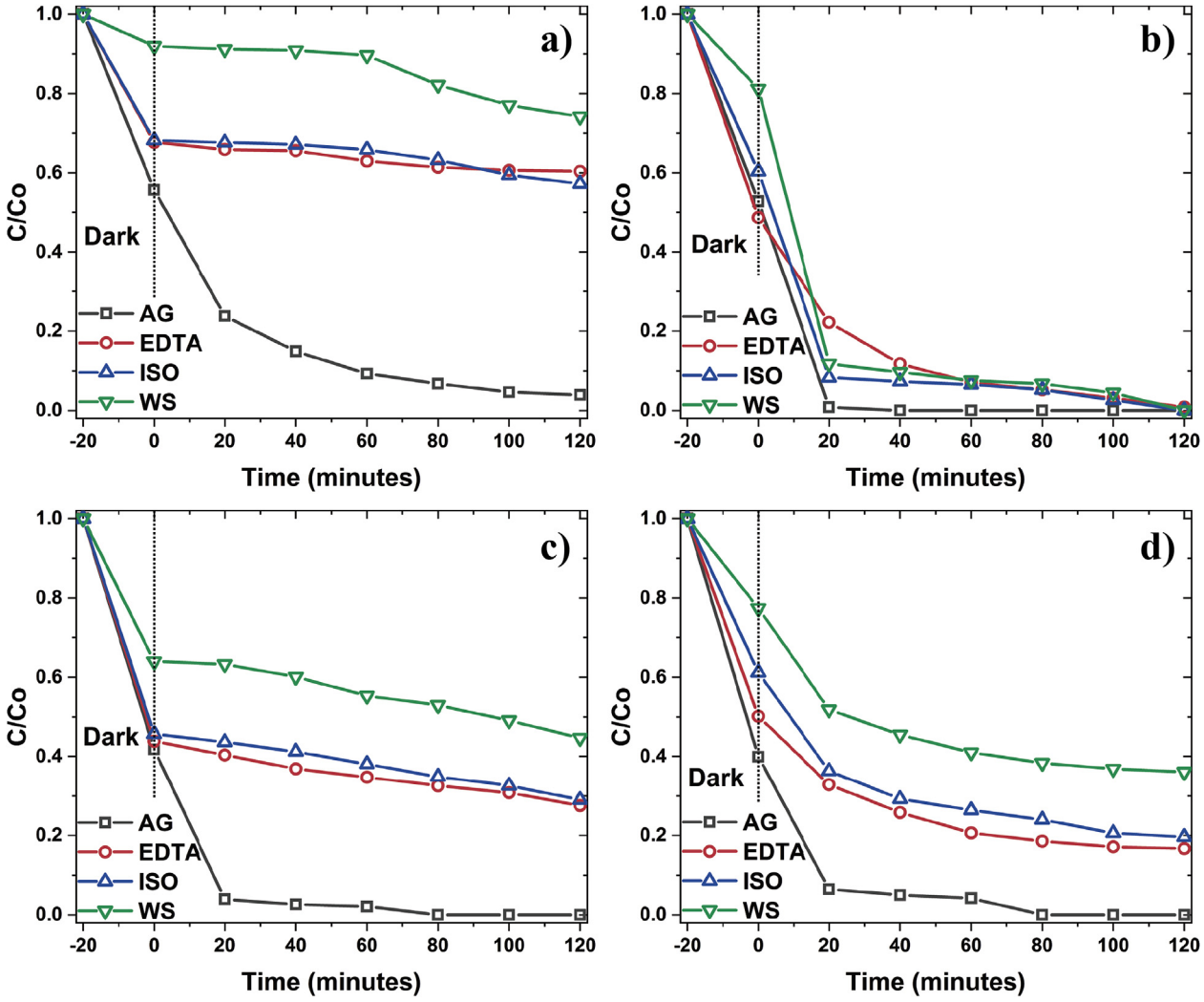

Fig. 9. MB dye concentration variation using scavengers for (a) pure, (b) Ag, (c) Zn and (d) Ag:Zn samples.

The use of particulate materials in photocatalytic activity requires their correct application so that there is no formation of secondary residues containing the photocatalyst. Thus, the ability of the material to be used in several consecutive catalytic cycles without the need for complex treatments is a prime factor for large-scale applications. Among the characteristics that make a material suitable for use in several consecutive cycles is the chemical stability and maintenance of the activity over the cycles [43]. The reuse tests in this work were performed by collecting the powders after the catalytic cycles by simple centrifugation which was then dried in the open air, and the powders were weighed and the catalyst/dye ratio maintained. Fig. 10a shows the degradation of the silver, zinc and co-doped samples which showed the best photocatalytic results, while Fig. 10b shows the diffractograms performed after the third cycle. As shown in Fig. 10a, the silver-doped sample loses its efficiency over the course of the cycles, so it loses 26% of its efficiency in the third cycle, while the zinc-doped and co-doped samples maintain virtually constant activity with each other. For the co-doped sample, a slight increase in photocatalytic efficiency is observed in the second cycle, followed by a reduction in the third cycle. This increase is associated with the small amount of silver present in the sample, where the radiation incidence tends to reduce silver on the surface of the particles, generating Ag^0 and producing the surface plasmon effect (SPR), while the reduction in efficiency occurs by the subsequent oxidation of these particles in silver oxide nanoparticles (AgO). Tun et al. [44] also reported the positive effect of reducing metallic silver on the surface of AgBr powders for photocatalytic activity, accompanied by a reduction in subsequent cycles. According to the diffractograms shown in Fig. 10b, the silver-doped sample shows the formation of AgO and Ca, characterized by the ICSD 27669 card with monoclinic system and space group C2/c (no. 15) and ICSD 44348 with cubic system and space group Fm-3m (no. 225), respectively. The emergence of these phases indicates the low chemical stability for photocatalytic applications using ultraviolet radiation, thus indicating the use of the co-doped sample, which presented second-best photocatalytic response and good chemical stability without the formation of secondary phases.

4. Conclusion

Diffractograms indicate that sonochemical synthesis is a fast, simple and efficient methodology for obtaining bare $CaWO_4$ nanoparticles and doped with silver and zinc without the formation of secondary phases. Defects resulting from doping act in altering the growth kinetics of the crystallites, resulting in a reduction in nanoparticle average diameter from 71.76 to 16.76 nm for pure and co-doped samples, respectively. The occupation of Ag

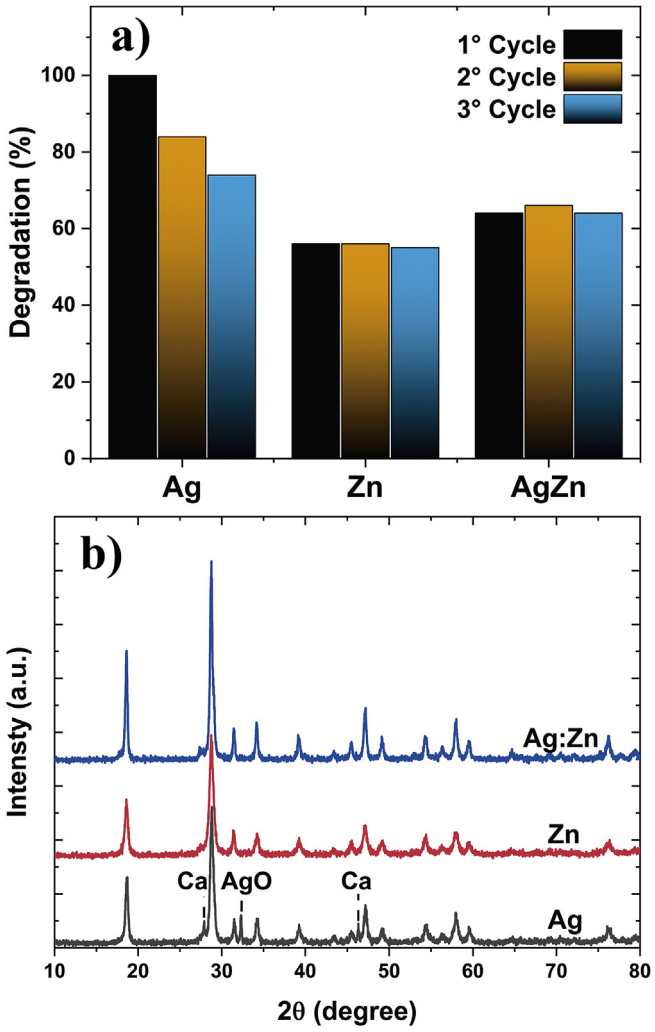

Fig. 10. (a) Reuse cycles and (b) DRX pattern after the third cycle for Ag, Zn and Ag:Zn samples.

and Zn ions at levels close to the conduction band shifts the band to higher energies, thus increasing the Egap. The photocatalytic and photoluminescent properties of semiconductor materials are directly related to the recombination ability of the electron/hole pairs. Thus, it can be assumed that the occupancy of levels close to the $CaWO_4$ conduction band by Ag and Zn cations act to reduce the recombination rate of these pairs, improving photocatalytic activity and reducing $CaWO_4$ photoluminescent capacity. The photocatalytic capacity of Ag and Zn-doped $CaWO_4$ powders is strongly influenced by the action of the holes (h^+), which act by generating reactive oxygen species and directly oxidizing the methylene blue dye chains. Reuse tests indicate that the silver-doped sample does not have good chemical stability, generating secondary phases over the course of the cycles. Thus, the co-doped sample is best suited for photocatalytic applications, as it has a good ability to degrade the methylene blue dye and maintain its chemical composition.

CRediT author statement

N. F. Andrade Neto: Conceptualization, Methodology, Software, Validation, Investigation, Data Curation, Writing - Original Draft, Visualization, Supervision, Project administration.

B. P. Dias: Methodology, Validation, Investigation, Visualization.

R. L. Tranquilin: Resources, Data Curation.

E. Longo: Resources, Data Curation.

M. Li: Resources, Data Curation.

M. R. D. Bomio: Conceptualization, Methodology, Validation, Investigation, Resources, Writing - Original Draft, Visualization, Supervision, Project administration, Funding acquisition.

F. V. Motta: Conceptualization, Methodology, Validation, Investigation, Resources, Writing - Original Draft, Visualization, Supervision, Project administration, Funding acquisition.

Declaration of competing interest

The authors declare that they have no known competing financial interests or personal relationships that could have appeared to influence the work reported in this paper.

Acknowledgment

This study was partially financed in part by the Coordenação de Aperfeiçoamento de Pessoal de Nível Superior - Brasil (CAPES/PROCAD) - Finance Code 2013/2998/2014 and the authors thanks to the financial support of the Brazilian research financing institution (CNPq) No. 307546/2014 and São Paulo Research Foundation (FAPESP - CDMF) No. 2013/07296-2.

Appendix A. Supplementary data

Supplementary data to this article can be found online at https://doi.org/10.1016/j.jallcom.2019.153617.

References

[1] N.F.A. Neto, L.M.P. Garcia, E. Longo, M.S. Li, C.A. Paskocimas, M.R.D. Bomio, F.V. Motta, Photoluminescence and photocatalytic properties of Ag/AgCl synthesized by sonochemistry: statistical experimental design, J. Mater. Sci. Mater. Electron. 28 (2017) 12273–12281.

[2] D.S. Babu, V. Srivastava, P.V. Nidheesh, M.S. Kumar, Detoxification of water and wastewater by advanced oxidation processes, Sci. Total Environ. 696 (2019) 133961.

[3] R. Anjali, S. Shanthakumar, Insights on the current status of occurrence and removal of antibiotics in wastewater by advanced oxidation processes, J. Environ. Manag. 246 (2019) 51–62.

[4] K. Sivagami, K.P. Sakthivel, I.M. Nambi, Advanced oxidation processes for the treatment of tannery wastewater, Journal of Environmental Chemical Engineering 6 (2018) 3656–3663.

[5] H. Su, C. Christodoulatos, B. Smolinski, P. Arienti, G. O'Connor, X. Meng, Advanced oxidation process for DNAN using UV/H_2O_2, Engineering 5 (2019) 849–854.

[6] L.M.P. Garcia, M.T.S. Tavares, N.F. Andrade Neto, R.M. Nascimento, C.A. Paskocimas, E. Longo, M.R.D. Bomio, F.V. Motta, Photocatalytic activity and photoluminescence properties of TiO_2, In_2O_3, TiO_2/In_2O_3 thin films multilayer, J. Mater. Sci. Mater. Electron. 29 (2018) 6530–6542.

[7] N.F. Andrade Neto, P. Zanatta, L.E. Nascimento, R.M. Nascimento, M.R.D. Bomio, F.V. Motta, Characterization and photoluminescent, photocatalytic and antimicrobial properties of boron-doped TiO_2 nanoparticles obtained by microwave-assisted solvothermic method, J. Electron. Mater. 48 (2019) 3145–3156.

[8] N.P. Singh, N.P. Singh, N.R. Singh, N.M. Singh, Photoluminescence studies of CdWO4:Sm^{3+} phosphor: concentration and annealing effect, Optik 144 (2017) 490–497.

[9] R.M. Abozaid, Z.Ž. Lazarević, N. Tomić, A. Milutinović, D. Šević, M.S. Rabasović, V. Radojević, Optical properties $CaWO_4$:Nd^{3+}/PMMA composite layered structures, Opt. Mater. 96 (2019) 109361.

[10] I. Rodríguez-Gutiérrez, E. Djatoubai, M. Rodríguez-Pérez, J. Su, G. Rodríguez-Gattorno, L. Vayssieres, G. Oskam, Photoelectrochemical water oxidation at FTO|WO_3@$CuWO_4$ and FTO|WO_3@$CuWO_4$|$BiVO_4$ heterojunction systems: an IMPS analysis, Electrochim. Acta 308 (2019) 317–327.

[11] Y. Wu, S. Zhou, T. He, X. Jin, L. Lun, Photocatalytic activities of $ZnWO_4$ and Bi@$ZnWO_4$ nanorods, Appl. Surf. Sci. 484 (2019) 409–413.

[12] N.F. Andrade Neto, Y.G. Oliveira, J.H.O. Nascimento, B.R. Carvalho, M.R.D. Bomio, F.V. Motta, Synthesis, characterization, optical properties investigation and reusability photocatalyst capacity of AgCl-xGO composite, J. Mater. Sci. Mater. Electron. 30 (2019) 15214–15223.

[13] C. Ayappan, B. Palanivel, V. Jayaraman, T. Maiyalagan, A. Mani, One-step hydrothermal synthesis of $CaWO_4$/α-Ag_2WO_4 heterojunction: an efficient

photocatalyst for removal of organic contaminants, Mater. Sci. Semicond. Process. 104 (2019) 104693.
[14] K. Somasundaram, C.K. Rastogi, I. Roy, P.C. Selvin, V. Sudarsan, Lanthanide ion induced phase decomposition of tetragonal $CaWO_4$, Mater. Res. Bull. 113 (2019) 133–140.
[15] Y. Song, S. Liang, F. Li, X. Wang, C. You, Y. Yang, The self-assembly mechanism of $CaWO_4$@$CaWO_4$:Dy^{3+} core/shell microspheres via a simple surfactant-free hydrothermal route, Mater. Lett. 161 (2015) 100–103.
[16] R. Chai, Y. Liu, G. Zhang, J. Feng, Q. Kang, In situ preparation and luminescence properties of $CaWO_4$ and $CaWO_4$:Ln (Ln=Eu^{3+}, Tb^{3+}) nanoparticles and transparent $CaWO_4$:Ln/PMMA nanocomposites, J. Lumin. 202 (2018) 65–70.
[17] E. Palmieri, A. Marcucci, G. Marcheselli, A. De Stefanis, R. Polini, Carbothermic reduction of scheelite ($CaWO_4$) doped with cobalt or nickel, Int. J. Refract. Metals Hard Mater. 59 (2016) 93–99.
[18] Y. Zhang, R. Fan, Q. Zhang, Y. Chen, O. Sharifi, D. Leszczynska, R. Zhang, Q. Dai, Synthesis of $CaWO_4$-biochar nanocomposites for organic dye removal, Mater. Res. Bull. 110 (2019) 169–173.
[19] S. Huang, Z. Lou, N. Zhu, H. Yuan, Comparison of photocatalytic activities between Er^{3+}/Yb^{3+} and Tm^{3+}/Yb^{3+} codoped ($CaWO_4$@(TiO_2/CaF_2)) near-infrared photocatalysts, Catal. Commun. 61 (2015) 6–10.
[20] B. Toby, EXPGUI, a graphical user interface for GSAS, J. Appl. Crystallogr. 34 (2001) 210–213.
[21] M. Patel, A. Chavda, I. Mukhopadhyay, J. Kim, A. Ray, Nanostructured SnS with inherent anisotropic optical properties for high photoactivity, Nanoscale 8 (2016) 2293–2303.
[22] B.D. Viezbicke, S. Patel, B.E. Davis, D.P. Birnie Iii, Evaluation of the Tauc method for optical absorption edge determination: ZnO thin films as a model system, Phys. Status Solidi 252 (2015) 1700–1710.
[23] N.F. Andrade Neto, Y.G. Oliveira, C.A. Paskocimas, M.R.D. Bomio, F.V. Motta, Increase of antimicrobial and photocatalytic properties of silver-doped PbS obtained by sonochemical method, J. Mater. Sci. Mater. Electron. 29 (2018) 19052–19062.
[24] N.F. Andrade Neto, P.M. Oliveira, R.M. Nascimento, C.A. Paskocimas, M.R.D. Bomio, F.V. Motta, Influence of pH on the morphology and photocatalytic activity of CuO obtained by the sonochemical method using different surfactants, Ceram. Int. 45 (2019) 651–658.
[25] D. Kumar, B.P. Singh, M. Srivastava, A. Srivastava, P. singh, A. Srivastava, S.K. Srivastava, Structural and photoluminescence properties of thermally stable Eu^{3+} activated $CaWO_4$ nanophosphor via Li+ incorporation, J. Lumin. 203 (2018) 507–514.
[26] M.D.P. Silva, R.F. Gonçalves, I.C. Nogueira, V.M. Longo, L. Mondoni, M.G. Moron, Y.V. Santana, E. Longo, Microwave-assisted hydrothermal synthesis of $Ag_2(W_{1-x}Mo_x)O_4$ heterostructures: nucleation of Ag, morphology, and photoluminescence properties, Spectrochim. Acta A Mol. Biomol. Spectrosc. 153 (2016) 428–435.
[27] L.S. Cavalcante, V.M. Longo, J.C. Sczancoski, M.A.P. Almeida, A.A. Batista, J.A. Varela, M.O. Orlandi, E. Longo, M.S. Li, Electronic structure, growth mechanism and photoluminescence of $CaWO_4$ crystals, CrystEngComm 14 (2012) 853–868.
[28] Y. Su, G. Li, Y. Xue, L. Li, Tunable physical properties of $CaWO_4$ nanocrystals via particle size control, J. Phys. Chem. C 111 (2007) 6684–6689.
[29] C.A. Schneider, W.S. Rasband, K.W. Eliceiri, NIH Image to ImageJ: 25 years of image analysis, Nat. Methods 9 (2012) 671–675.
[30] M.A. Ávila-López, E. Luévano-Hipólito, L.M. Torres-Martínez, CO_2 adsorption and its visible-light-driven reduction using CuO synthesized by an eco-friendly sonochemical method, J. Photochem. Photobiol. A Chem. 382 (2019) 111933.
[31] Z. Lou, M. Cocivera, Cathodoluminescence of $CaWO_4$ and $SrWO_4$ thin films prepared by spray pyrolysis, Mater. Res. Bull. 37 (2002) 1573–1582.
[32] R. Grasser, A. Scharmann, K.R. Strack, On the intrinsic nature of the blue luminescence in $CaWO_4$, J. Lumin. 27 (1982) 263–272.
[33] Y. Zhang, N. Holzwarth, R. Williams, Electronic band structures of the scheelite materials and, Phys. Rev. B Condens. Matter Mater. Phys. 57 (1998) 12738–12750.
[34] A. Sarkar, S. Ghosh, S. Chaudhuri, A.K. Pal, Studies on electron transport properties and the Burstein-Moss shift in indium-doped ZnO films, Thin Solid Films 204 (1991) 255–264.
[35] A. Taoufyq, V. Mauroy, T. Fiorido, F. Guinneton, J.-C. Valmalette, B. Bakiz, A. Benlhachemi, A. Lyoussi, G. Nolibe, J.-R. Gavarri, Photoluminescence properties of $CaWO_4$ and $CdWO_4$ thin films deposited on SiO_2/Si substrates, J. Lumin. 215 (2019) 116619.
[36] K.Y. Jung, J.C. Lee, D.S. Kim, B.-K. Choi, W.-J. Kang, Co-doping effect of monovalent alkali metals on optical properties of CeO_2:Eu nanophosphor prepared by spray pyrolysis and application for preparing pearlescent pigments with red emission, J. Lumin. 192 (2017) 1313–1321.
[37] J. Xia, H. Li, H. You, Z. Wu, J. Chen, Z. Lu, L. Chen, M. Wang, Y. Jia, Effects of Fe doping on photoluminescent and magnetic properties of $CaTiO_3$:Eu^{3+}, Ceram. Int. 44 (2018) 21530–21532.
[38] L. Xu, G. Zheng, F. Xian, Y. Liu, Tailoring the photoluminescent property of ZnO/Ag nanocomposite thin films based on a thermal treatment, J. Lumin. 198 (2018) 296–301.
[39] K. Li, C. Dong, Y. Zhang, H. Wei, F. Zhao, Q. Wang, Ag–AgBr/$CaWO_4$ composite microsphere as an efficient photocatalyst for degradation of Acid Red 18 under visible light irradiation: affecting factors, kinetics and mechanism, J. Mol. Catal. A Chem. 394 (2014) 105–113.
[40] B. An, Y. Xin, R. Niu, J. Lu, E. Wang, K. Han, Hardening Cu-Ag composite by doping with Sc, Mater. Lett. 252 (2019) 207–210.
[41] R.K. Mishra, V.B. Kumar, A. Victor, I.N. Pulidindi, A. Gedanken, Selective production of furfural from the dehydration of xylose using Zn doped CuO catalyst, Ultrason. Sonochem. 56 (2019) 55–62.
[42] A.A.G. Santiago, N.F. Andrade Neto, E. Longo, C.A. Paskocimas, F.V. Motta, M.R.D. Bomio, Fast and continuous obtaining of Eu^{3+} doped CeO_2 microspheres by ultrasonic spray pyrolysis: characterization and photocatalytic activity, J. Mater. Sci. Mater. Electron. 30 (2019) 11508–11519.
[43] R. Qian, H. Zong, J. Schneider, G. Zhou, T. Zhao, Y. Li, J. Yang, D.W. Bahnemann, J.H. Pan, Charge carrier trapping, recombination and transfer during TiO_2 photocatalysis: an overview, Catal. Today 335 (2019) 78–90.
[44] J. Trawiński, R. Skibiński, Rapid degradation of clozapine by heterogeneous photocatalysis. Comparison with direct photolysis, kinetics, identification of transformation products and scavenger study, Sci. Total Environ. 665 (2019) 557–567.